AGU PUBLICATIONS

Global Biogeochemical Cycles

RESEARCH ARTICLE
10.1002/2013GB004585

Key Points:
- Surface pCO2 measurements are analyzed for global CO2 air-sea flux trends
- Model and data-based information is combined using Bayesian probability
- Interannual variability is included to prevent bias from sampling errors

Supporting Information:
- Supplemental Figures S1–S8 and Tables S1–S4

Correspondence to:
J. D. Majkut,
jmajkut@princeton.edu

Citation:
Majkut, J. D., J. L. Sarmiento, and K. B. Rodgers (2014), A growing oceanic carbon uptake: Results from an inversion study of surface pCO$_2$ data, *Global Biogeochem. Cycles*, *28*, 335–351, doi:10.1002/2013GB004585.

Received 11 FEB 2013
Accepted 23 FEB 2014
Accepted article online 26 FEB 2014
Published online 1 APR 2014

A growing oceanic carbon uptake: Results from an inversion study of surface pCO$_2$ data

Joseph D. Majkut[1], J. L. Sarmiento[1], and K. B. Rodgers[1]

[1] Atmospheric and Oceanic Sciences Program, Princeton University, Princeton, New Jersey, USA

Abstract Concerted community efforts have been devoted to producing an authoritative climatology of air-sea CO_2 fluxes, but identifying decadal trends in CO_2 fluxes has proven to be more challenging. The available surface pCO$_2$ estimates are too sparse to separate long-term trends from decadal and seasonal variability using simple linear models. We introduce Markov Chain Monte Carlo sampling as a novel technique for estimating the historical pCO$_2$ at the ocean surface. The result is a plausible history of surface pCO$_2$ based on available measurements and variability inferred from model simulations. Applying the method to a modern database of pCO$_2$ data, we find that two thirds of the ocean surface is trending toward increasing uptake of CO_2, with a mean (year 2000) uptake of 2.3 $\pm$ 0.5 PgC yr^{-1} of anthropogenic carbon and an increase in the global annual uptake over the 30 year time period of 0.4 $\pm$ 0.1 PgC yr^{-1} decade^{-1}. The results are particularly interesting in the Southern Ocean, where we find increasing uptake of carbon over this time period, in contrast to previous studies. We find evidence for increased ventilation of deep ocean carbon, in response to increased winds, which is more than offset by an associated surface cooling.

1. Introduction

The flux of CO_2 at the air-sea interface controls atmospheric CO_2 concentrations on centennial timescales and is an important term in the year-to-year carbon budget of the atmosphere. Currently, the ocean absorbs CO_2 from the atmosphere. Each year the uptake is equivalent to about 30% of annual fossil fuel emissions [*Sarmiento et al.*, 2010]. The flux amounted to 2.0 $\pm$ 1.0 PgC yr^{-1} in the decade surrounding the year 2000, according to multiple estimation techniques [*Takahashi et al.*, 2009; *Wanninkhof et al.*, 2013], though other estimates show smaller uncertainties, 2.0 $\pm$ 0.6 PgC yr^{-1} [*Gruber et al.*, 2009].

Recently, analysis of the atmospheric carbon content has shown that the combined land-ocean sink of CO_2 from the atmosphere has grown from 2.4 $\pm$ 0.8 PgC yr^{-1} in 1960 to 5.0 $\pm$ 0.9 PgC yr^{-1} in 2010 [*Ballantyne et al.*, 2012]. Partitioning the growth into terrestrial and oceanic components will be helpful in developing an understanding of the dynamics that lead to trends in the land and ocean sinks and how they affect the response of the climate system to anthropogenic forcing through carbon cycle feedbacks [*Friedlingstein et al.*, 2006]. In the future, if we wish to have a system that monitors the carbon budget between the atmosphere, terrestrial biosphere, and ocean, having an updated estimate of the air-sea flux and an understanding of its trends will be essential.

The scarcity of measurements makes it difficult to examine trends in the air-sea CO_2 flux [*Doney et al.*, 2009a] and estimates of the trend in the global flux vary significantly [*Wanninkhof et al.*, 2013]. Studies of the trends in the oceanic uptake of CO_2 largely hinge on surface measurements of pCO$_2$. Since the air-sea CO_2 flux is based on the disequilibrium in the partial pressure of the gas, pCO$_2$ in µatm yr^{-1}, a common metric of the flux trend is the rate of change of pCO$_2$ in the sea surface compared to the atmospheric pCO$_2$ growth rate. *Fay and McKinley* [2013] calculated trends in surface pCO$_2$, globally but divided into ocean biomes, and showed that trends in pCO$_2$ from the surface measurements are strongly influenced by decadal variability and that the multidecadal trend, measured over 30 years, in surface pCO$_2$ for the tropics and subtropics is consistent with or slightly slower than the atmospheric growth rate. Time series at two of the most highly sampled oceanic regions, from the ocean stations BATS and HOT, also show that the surface ocean pCO$_2$ growth rate is similar to the atmospheric growth rate [*Bates*, 2007; *Dore et al.*, 2009].

In the Subtropical North Pacific, *Takahashi et al.* [2006] argued that the increase in the surface pCO$_2$ in the Subtropical North Pacific has been slower than that of the atmosphere over the last few decades. In the North Atlantic, surface pCO$_2$ trends imply a decreasing air-sea flux. *Schuster and Watson* [2007] found regions of decreasing ocean uptake, between 1994–1995 and 2002–2004, in the Atlantic Basin between 20°N and 65°N. *Feely et al.* [2006] used surface pCO_2 data to show that the degassing flux from the Equatorial Pacific increased in the mid-1990s, concurrent with the shift in the Pacific Decadal Oscillation in 1997. *Le Quéré et al.* [2010] showed that Southern Ocean pCO_2 was increasing faster than the atmospheric value in the winter months from 1981 to 2007. The trends that are implied by these local studies might point to substantial changes in the oceanic CO_2 uptake and it is important to understand how the global trend emerges from the regional trends.

Takahashi et al. [2009] have collected a substantial set of surface pCO_2 measurements and used them to build an authoritative atlas of the annual cycle of pCO_2 in the surface ocean and implied climatology of air-sea CO_2 flux. The observations that were used to make the climatology, mostly underway measurements of pCO_2 from research cruises and volunteer ships of opportunity, have been released as a database, LDEO2010, for public download [*Takahashi et al.*, 2012]. More recently, the efforts of *Pfeil et al.* [2012] and *Sabine et al.* [2012] have resulted in the Surface Ocean CO_2 Atlas (SOCAT) database and gridded products, a quality controlled and publicly documented collection of surface pCO_2 measurements. These initiatives allow for the continued use of surface measurements as a source of information about the surface ocean carbon system. For us, the availability of these data provides an opportunity for a global analysis of trends in the sea surface pCO_2 and the air-sea CO_2 flux over the past few decades.

Despite the size of the LDEO2010 database, the available surface pCO_2 measurements are sparse. The resultant climatology [*Takahashi et al.*, 2009] is reported on a grid of 5° (longitude) × 4° (latitude) boxes. The observations cover less than 5% of the values needed if one wishes to have a pCO_2 history on that grid with monthly values from 1980 to 2005. Data availability is highest in the North Atlantic and North Pacific. Large parts of the Southern Hemisphere, tropics, and subtropics are sampled with a seasonal bias, once or twice or not at all. The small number of available measurements over the whole globe makes it difficult to separate trends from interannual variability, the seasonal cycle, and transient variations in each region of the ocean.

We introduce the Markov Chain Monte Carlo (MCMC) method in section 2 below. We then demonstrate the MCMC method on a synthetic data set and finally use it to estimate pCO_2 time series and trends using data from the LDEO2010 database. Section 3 shows the estimated trends, sensitivity to the representation of seasonal and interannual variability, and the fluxes that result from the pCO_2 time series associated with our inversions. Lastly, we discuss the implications of the inversion for the ocean carbon sink and the global carbon cycle.

2. Methods

Here we describe the formulation of the simple model we use for the surface pCO_2 and the Markov Chain Monte Carlo inversion technique. Then we discuss how we implement the two using the LDEO2010 data. The MCMC inversion is a Bayesian technique and requires us to impose an a priori distribution for the parameters in the pCO_2 model. The a priori distribution represents our best knowledge about the model before it is inverted with data. In this section, we describe how we estimate the prior distribution for the pCO_2 model from a selection of ocean general circulation model simulations with biogeochemistry, which are described in Table 1.

Briefly, the MOM4p1-BLING model we used for prior information is based on the NOAA Geophysical Fluid Dynamics Laboratory (GFDL) Modular Ocean Model version 4.1 [*Griffies et al.*, 2004] with 3° horizontal resolution. The circulation model is coupled to the Biology Light Iron Nutrient and Gas (BLING) idealized biogeochemistry model [*Galbraith et al.*, 2011]. This model configuration was included in several variations, with simulations forced by different reanalysis products: CORE-II [*Large and Yeager*, 2009], ERA-40 [*Uppala et al.*, 2005] and NCEP1 [*Kalnay et al.*, 1996] and a simulation forced with a climatology derived from CORE-II. Additionally, we used two simulations from the latest versions of the NEMO-PISCES model [*Aumont and Bopp*, 2006], using the ORCA2 configuration of NEMO Version 3.2, with 2 degree horizontal resolution and 31 vertical levels. This model was forced with the DRAKKAR Forcing Set 4.1, or DFS4.1 [*Brodeau et al.*, 2010].

2.1. Estimating pCO_2 Time Series

We implement and perform inversion of a simple model for the surface water pCO_2, shown in equation (1), which has terms for four modes of variability with monthly resolution:

$$pCO_2^{sea}(x,y,t) = A(x,y) \cdot t + B(x,y) + C(x,y) \cdot \mathrm{SEAS}(x,y,T) + D(x,y) \cdot \mathrm{IAV}(x,y,t) \tag{1}$$

Table 1. Coupled Ocean-Biogeochemistry Models

Model	Forcing	Resolution	Dates
MOM4p1-BLING [*Griffies et al.*, 2004; *Galbraith et al.*, 2011]	CORE-II [*Large and Yeager*, 2009]	3°	1980–2006
	CORE-II-NY	3°	1960–1980[a]
	NCEP-1 [*Kalnay et al.*, 1996]	3°	1980–2006
	ERA-40 [*Uppala et al.*, 2005]	3°	1980–2003
OPA-PISCES (A) [*Aumont and Bopp*, 2006]	DRAKKAR [*Brodeau et al.*, 2010]	2°	1980–2006
OPA-PISCES (B)[b]	DRAKKAR [*Brodeau et al.*, 2010]	2°	1980–2006

[a]This simulation was run with the atmospheric CO_2 from 1980 to 2006, but with the climatological forcing of the ocean circulation.
[b]The two versions of the OPA-PISCES model use different parameterizations of mixed layer turbulence as in *Rodgers et al.* [2013].

The coefficient of the first term, A in μatm yr^{-1}, is meant to represent the multidecadal linear trend with time. We generally expect A to have a positive value, as a warming ocean that is also absorbing anthropogenic CO_2 from the atmosphere should exhibit increasing pCO_2. B gives the June 1995 value for pCO_2 in µatm; t is referenced to that month. The constant term allows for regional differences in the mean carbon content of the surface ocean. The seasonal and interannual variabilities about that linear model are represented by the remaining two terms. In this case, we consider seasonal variations to be a climatological repeating cycle, SEAS in µatm, based on the average annual cycle for a grid box. The time dependence of this term is climatological, and thus, it depends on the repeating monthly time grid, T. The monthly value of SEAS is calculated as the average deviation from the linear trend for each month, from 1980 to 2006. The interannual term, IAV in µatm yr^{-1}, represents mean year-to-year variability, such as decadal trends, and interannual variability at monthly timescales, such as an early spring bloom or the increasing seasonality in pCO_2. Both the seasonal and interannual terms have zero averages over the whole time period. Thus, the trend parameter, A, should fully represent the changes in surface pCO_2 over the 30 year window. Figure 1a shows how the model represents the surface pCO_2 data in the Eastern Pacific 5° × 4° box centered at (132.5°W, 16°N), with different coefficients from before and after inversion.

Previous attempts to estimate pCO_2 as a function of time have generally been limited to a simple linear function including the $A(x, y) \cdot t$ and $B(x, y)$ terms and some representation of the seasonal cycle, our $C(x, y) \cdot \mathrm{SEAS}(x, y, T)$, *Takahashi et al.* [2009]; and using ordinary least squares to estimate the model parameters. Our contribution is to add the interannual variability, $D(x, y) \cdot \mathrm{IAV}(x, y, t)$ and to implement a Bayesian inversion scheme that allows us to include prior estimates as constraints on the model parameters.

2.2. MCMC Inversion

The inversion scheme we implement is a version of Markov Chain Monte Carlo sampling. Each of the parameters (A, B, C, D) in equation (1) is subject to Bayesian inversion using the observations in LDEO2010 and the

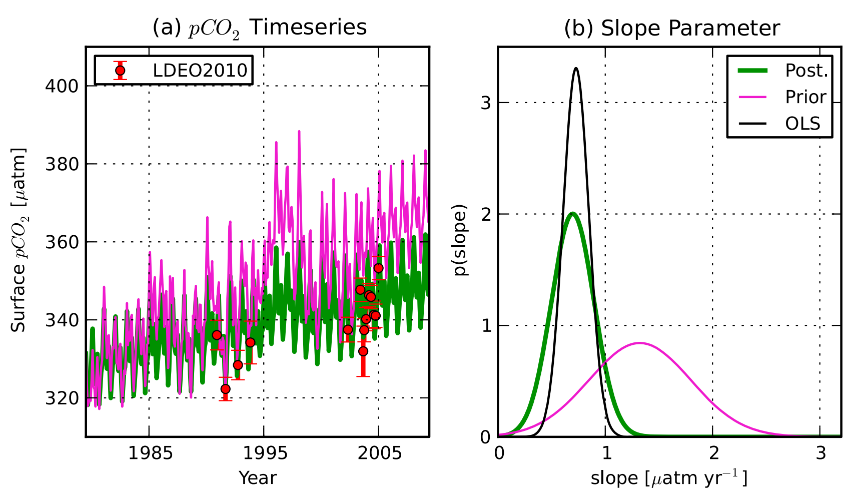

Figure 1. These figures show (a) pCO_2 time series and (b) the distributions associated with the parameter A for a grid cell in the Eastern Pacific. The green line shows the posterior estimate for the pCO_2 time series and the magenta shows the prior estimate. The red dots indicate the monthly averaged measurements from LDEO2010.

pCO$_2$ values predicted by the simple model. The prior distribution for the parameters (A, B, C, D) is updated with the available observations to yield posterior distributions for each of the parameters. Thus, the inversion can change the probability distributions governing the trend, initial value, and the amplitude of the prescribed seasonal and interannual variability. In this implementation, it cannot change the phase of the seasonal cycle or modify the model-based estimate of a singular event such as a particular El Niño.

The MCMC performs an iterative random walk of the parameter space of the pCO$_2$ model to arrive at an optimal parameter estimate given the prior information and available data. Given a seed vector x_n in parameter space (A, B, C, D), the MCMC algorithm randomly selects a nearby point as a proposed step, x_{n+1}, and uses a specific decision criterion to accept or reject that next step based on the misfit of the observations and model predictions and the prior probability assigned to that point in parameter space. If the proposed step is accepted, then the walk moves to that position and starts again, otherwise, it starts again from the current position.

Our implementation of the MCMC uses the Metropolis-Hastings decision criterion. The proposed step is approved with probability, α, determined by

$$\alpha = \min\left[1, \frac{p(x_{n+1})L(M|x_{n+1})}{p(x_n)L(M|x_n)}\right]. \tag{2}$$

Under this decision criterion, the set of positions occupied during the random walk converge to a sampling of the posterior distribution of the parameters given the observations [*Hastings*, 1970]. In equation (2), $p(x)$ is the prior probability of the point x in parameter space. $L(M|x)$ is the likelihood function for the parameter given the data available. The likelihood is the probability of obtaining the pCO$_2$ measurements M from LDEO2010, in the case that the true parameters of the model are located at x. If the misfit between the modeled pCO$_2$ at the parameter values in x is larger than the error associated with the measurements, then the likelihood will be low at that point. The likelihood calculation requires the error covariance matrix for the observations M, and M varies in size depending on how many observations are available in each grid box of the inversion.

Under the probabilistic metropolis rule, the random walk will tend to move toward areas of parameter space where both the prior probability and the model likelihood are high and thus a good fit of the data. That tendency generates the sampling of the posterior distribution. Figure 1b demonstrates how inversion with the data in LDEO changes the model-based prior distribution for the slope parameter A. The MCMC inversion both changes the mean and the standard deviation of the parameter's distribution, indicating that the data has substantial information about this parameter in that region.

2.3. Calculating Fluxes From pCO$_2$

The air-sea flux of CO$_2$ is a function of the difference in pCO$_2$ between the two mediums, ΔpCO$_2$, and an exchange velocity, k_w, according to the form in equation (3).

$$\Phi = k_w \Delta p\mathrm{CO}_2 \tag{3}$$

The gas exchange velocity is calculated as a function of the squared wind speed at 10 m above sea level, the solubility of CO$_2$ in seawater, α, and the local Schmidt number, Sc [*Wanninkhof et al.*, 2009].

$$k_w = \gamma \cdot \alpha \cdot \left(\frac{\mathrm{Sc}}{600}\right)^{-0.5} \cdot U_{10}^2 \tag{4}$$

The value of γ in these calculations is 0.27 [*Sweeney et al.*, 2007]. In the year 2000, we use the gas exchange piston velocity from *Takahashi et al.* [2009] so that the fluxes are directly comparable to those from the climatology. We then diagnose the time variation in k_w from the reanalysis forced simulation with MOM4p1-BLING.

In this work, we define ΔpCO$_2$ to be positive for excess pCO$_2$ in the ocean relative to the atmosphere, such that a positive flux is out of the ocean and a negative flux is into the ocean.

$$\Delta p\mathrm{CO}_2 = p\mathrm{CO}_2^{\mathrm{sea}} - p\mathrm{CO}_2^{\mathrm{air}} \tag{5}$$

We use the atmospheric mixing ratio of CO$_2$ from the global monitoring stations at Mauna Loa and the South Pole, assigning the Mauna Loa value north of Hawaii and linearly interpolating between Hawaii and the South pole for the rest of the globe [*Keeling et al.*, 2001]. This was the same atmospheric pCO$_2$ that was used to force the MOM4p1-BLING model simulations. The difference between fluxes calculated with this atmospheric pCO_2 and the atmospheric pCO_2 from *Takahashi et al.* [2009] in the year 2000 are negligible. We also use local sea level pressure to calculate the atmospheric pCO_2 at the sea surface. We assume that the atmospheric CO_2 is zonally homogeneous. Thus, the estimates of the air-sea carbon flux can follow directly from estimates of the surface water pCO_2. Likewise, trends in the air-sea carbon flux can be related to the relative trends in pCO_2 in the sea surface and lower atmosphere. We assume a preindustrial air-sea CO_2 flux of 0.4 ± 0.2 PgC yr^{-1} out of the ocean when calculating the global anthropogenic CO_2 uptake as in *Takahashi et al.* [2009].

2.4. Defining Inversion Parameters

Each of the parameters (A, B, C, D) in the pCO_2 model in equation (1) needs to be supplied with a prior distribution. We assume that the parameters are independent and normally distributed when assigning the prior. For the trend and intercept (A, B), we generate the prior mean and standard deviation using an ensemble of six ocean general circulation model simulations that were coupled with biogeochemistry. The physical circulation of the individual models was forced with atmospheric reanalysis products and the ocean-biogeochemistry models were forced with atmospheric CO_2 concentrations. We use the models as different representations of how the ocean biogeochemistry would be expected to respond to the increasing atmospheric concentrations of CO_2 and the climate experienced over 1980–2006. Each of the models was spun-up from preindustrial conditions with the historical atmospheric CO_2 and forced by a climatological year (monthly averaged values from 1959 to 1979 with imposed 6-hourly variability) of the atmospheric forcing until the start of the atmospheric reanalysis time period in the 1950s.

We used ordinary least squares to calculate the linear slope and mean value for each model's time series of pCO_2 in the $5° \times 4°$ grid boxes and then calculated the ensemble mean and standard deviation for both parameters to form the prior distributions. The number of samples in this case is small and the sample standard deviation that results is not robust. Thus, we increased the standard deviation of the ensemble by a factor of 3 to define the prior standard deviation of A. This is consistent with setting the standard deviation at the upper range of the confidence interval for the true standard deviation between the 90 and 95% levels. The prior standard deviation for the geographical mean, B, is assumed to be the sample standard deviation from the ensemble. The construction of the SEAS and IAV signals is described in the next paragraphs.

The seasonal variability can be diagnosed from observations for some areas [*Takahashi et al.*, 2009], but sampling scarcity makes it hard to do so for the global ocean. The seasonal cycle can also be estimated with harmonic functions for boxes of a few degrees [*Schuster and Watson*, 2007] or basin-scale regions [*Fay and McKinley*, 2013], but data scarcity is again a problem. Coupled ocean-ecosystem models are attractive because they offer pCO_2 time series without gaps, but the modeled seasonal cycle can be biased [*Woloszyn et al.*, 2011]. In our inversion, we use the seasonal cycle from the MOM4.1-BLING simulation and the *Takahashi et al.* [2009] seasonal cycle and compare the results between the two inversions to examine the sensitivity to the imposed seasonal cycle. The modeled seasonal cycle is defined for each month, is set to be a climatology of deviations from the annual mean, and is a repeating cycle for the 30 year time period. Likewise, the climatological seasonal cycle based on observations has no variation between years, but it is constructed from interpolated observations from the LDEO2010 database.

In this work, the interannual variability was taken from the MOM4.1-BLING simulations under CORE-II forcing. The CORE-II forced simulation was chosen for the IAV term because of the improved representation of the wind forcing fields in the Southern Ocean and Equatorial Pacific [*Large and Yeager*, 2009]. The interannual term, IAV(x, y, t), is defined for each month as the difference between the MOM4.1-BLING pCO_2 and the ordinary least squares linear fit against the model plus the repeating seasonal cycle from the model. We chose to use the interannual variability from the reanalysis forced model because the signals would be "time-stamped" in the same way as the data in LDEO2010. If the data show a strong response to the El Niño in 1997–1998, for instance, that response should be adjusted for using the modeled response from the MOM4p1-BLING simulation as the surface forcing reflects the conditions at that time. Since the CORE-II forcing product ends in 2005, interannual variability after that year is set to zero. The effect of introducing the IAV term from the forced-model simulations is examined in the sensitivity analysis. The imposed seasonal cycle and interannual variability might be inconsistent with the observations of surface pCO_2 and thus introduce additional bias. Our framework allows for the scaling parameter for each, (C, D) in equation (1), to be subject to inversion. In this framework, the imposed signals can be muted or amplified to provide a better fit

Table 2. Coupled CMIP5 Ocean-Atmosphere-Biogeochemistry Models[a]

Model	Simulation	Resolution
HadGEM2-CC	r1i1p1	1.9 × 1.3
HadGEM2-CC	r2i1p1	1.9 × 1.3
HADGEM2-ES	r1i1p1	1.9 × 1.3
GISS-E2-R	r1i1p1	1.0 × 1.3
GFDL-ESM2M	r1i1p1	1.0 × 1.0

[a]See *Bellouin et al.* [2011], *Schmidt et al.* [2006], and *Dunne et al.* [2013].

to the observations. For the prior of the amplitude parameters (C, D), we assume a normal distribution with mean of 1.0 and standard deviation 1.0. This prior was assigned for all grid cells and both time series and assumes a high uncertainty in the imposed signals.

To calculate the likelihood, $L(M|x)$, it is necessary to have an error covariance matrix for the observations in LDEO2010. In this application, the data vector, M, is the array of all of the monthly averaged pCO_2 measurements from LDEO2010 for each cell. We assume that the errors are unbiased, independent, and normally distributed. The standard deviation of the individual distributions is set equal to the monthly sample standard deviation in each grid cell. In cases where the standard deviation is undefined or very small, we set a floor for the error at the instrumental precision of 3.0 μatm [*Takahashi et al.*, 2009].

2.5. Demonstration Study

In this section we use an Observing System Simulation Experiment (OSSE) to demonstrate the benefits of the MCMC method and the importance of including the IAV term for properly calculating to pCO_2 trend. We choose output from the NOAA GFDL ESM2M historical simulation for Coupled Model Intercomparison Project Phase 5 (CMIP5) [*Dunne et al.*, 2012, 2013] for the “true” pCO_2. Then, the space-time coordinates of the observations in LDEO2010 are used to sample the ESM2M and to infer trends from this subsampling of the model. We add an unbiased normally distributed error term to each synthetic observation with the same standard deviation that we assign to the measurements in the data-based inversion. The MCMC is initialized with a prior based on an ensemble of five CMIP5 historical simulations (for a description, see Table 2). The prior was constructed in the same way as the prior for the LDEO2010 inversion, with the climate models in place of the reanalysis forced models. The trends inferred from ordinary least squares and the MCMC inversion applied to this synthetic database are then compared with the full trend explicitly resolved by ESM2M.

To illustrate the importance of representing the interannual variability for capturing the true slope, we separate the slope calculation into different components. We find A and B by fitting:

$$pCO_2(x, y, t)_{\text{full}} = A_{\text{full}}(x, y) \cdot t + B_{\text{full}}(x, y) \tag{6}$$

where A_{full} and B_{full} are the “true” value for the parameters obtained from the fully sampled model output. We then define the signals SEAS and IAV from the residuals of that fit:

$$pCO_2(x, y, t)_{\text{full}} - \left[A_{\text{full}}(x, y) \cdot t + B_{\text{full}}(x, y))\right] = \text{SEAS}(x, y, T) + \text{IAV}(x, y, t). \tag{7}$$

We now subsample the model output at the LDEO2010 points, correcting for SEAS but not IAV,

$$pCO_2(x, y, t)_{\text{ldeo}} - \text{SEAS}(x, y, T) \sim A_{\text{sub}}(x, y, t) \cdot t + B_{\text{sub}}(x, y), \tag{8}$$

such that there is potentially a bias imposed by not correcting for the subsampling of the IAV signal. Correcting for that bias is one of the novelties of this work. Since the model output has full resolution, we can directly estimate the bias that results by fitting a linear model to the subsampled interannual variability,

$$\text{IAV}(x, y, t)_{\text{ldeo}} \sim A_{\text{iav}}(x, y, t) \cdot t + B_{\text{iav}}(x, y). \tag{9}$$

Figure 2a shows the fully sampled model trend A_{full} and Figure 2c shows the least squares fit to the seasonally adjusted synthetic data set, A_{sub}. The A_{sub} estimates vary significantly from cell to cell and are not representative of the true value from the climate model simulation. Figure 2e shows the effect of the undersampling of the interannual variability on the least squares trend estimation, A_{iav}. This is the level by which the trend estimates in Figure 2c are biased by undersampling. Figure 2f shows that when the bias term is removed, $A_{\text{sub}} - A_{\text{iav}}$, then the true pCO_2 evolution is nearly achieved for the whole globe.

The trend estimates from the MCMC inversion of the synthetic data, A_{mcmc}, are shown in Figure 2b, where they compare favorably to the true slope exhibited by ESM2M. After updating with the synthetic

10.1002/2013GB004585

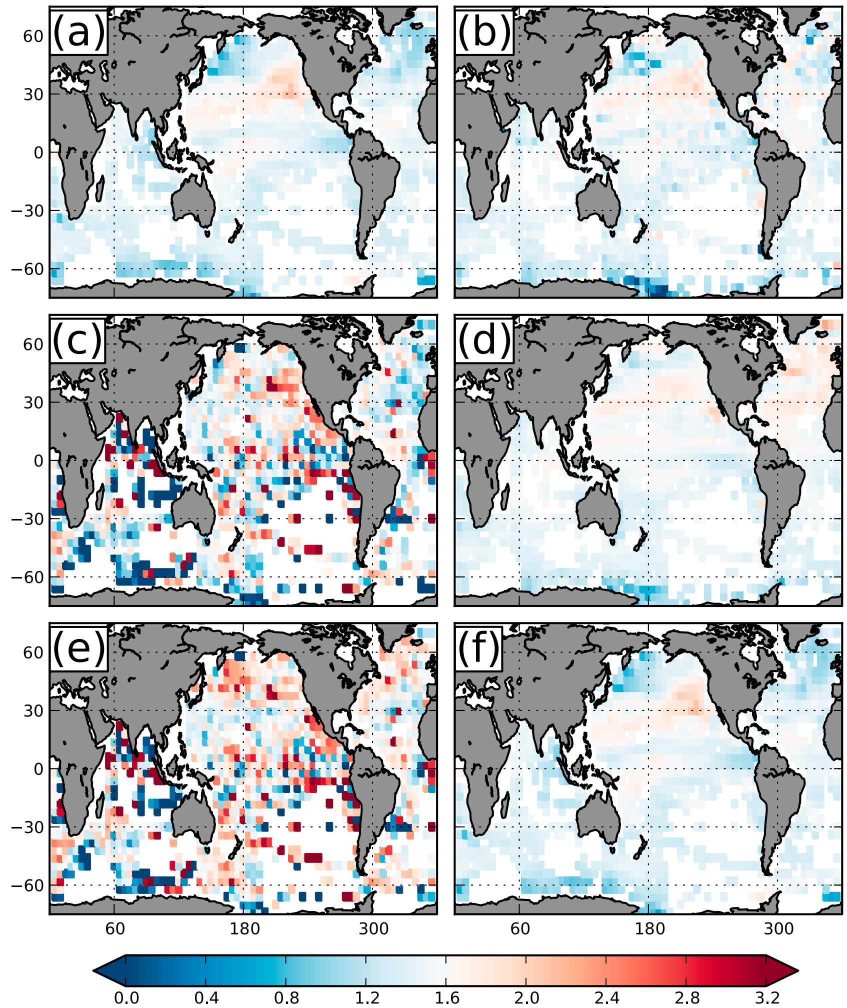

Figure 2. This figure shows different pCO_2 slope estimates, in µatm yr^{-1}, for the GFDL ESM2M verification experiment. (a) The true case is the slope of the fully sampled model pCO_2, A_{full}. (b) The same slope calculated by MCMC, A_{mcmc}, with the synthetic LDEO2010 measurements. (c) The subsampled slope A_{sub}, calculated from the synthetic data with ordinary least squares. (d) The prior used to initialize the MCMC from Figure 2b. (e) A_{iav}, the bias in slope that results when subsampling the IAV term. Lastly, (f) the sum of A_{sub} and A_{iav}.

database, using the same sampling as described in sections 2 and 3, the MCMC technique reduces the root-mean-squared error of the trend estimates by 95% compared to the A_{sub} estimates in Figure 2c. The majority of that reduction comes from including the interannual variability terms. The differences between the two estimates, A_{sub} and A_{mcmc}, shows that the MCMC inversion is a practical technique for including the interannual variability and avoiding the bias A_{iav} in the final estimates.

The difference between A_{mcmc}, in Figure 2b, and the compensated least squares estimate $A_{sub} - A_{iav}$, in Figure 2f, shows the potential pitfalls of the MCMC method for trend estimation. For example, the prior slope estimate influences the final slope estimate of the MCMC. When the prior and true slopes are aligned, the MCMC returns a reasonable slope, as occurs over much of the Southern Hemisphere in this test. When the prior estimate and true slope are not aligned, the MCMC estimate can only reveal the true slope if the available measurements and imposed variability provide sufficient constraint. In this test case, the mean slope of the prior has a different sign, relative to the atmospheric growth rate, than the true case in substantial areas of the North Pacific and North Atlantic (265 cells). The MCMC inversion with synthetic data decreases these errors by over half (fixing 156 cells) but does not return the correct sign in continuous regions of the Western North Atlantic or Western Subtropical Pacific. Globally, however, the MCMC inversion reduces the bias in the prior slope estimate from 0.1 μatm yr^{-1} to 0.04 μatm yr^{-1} and the MCMC-estimated slope distribution captures the true value within in the $\pm 2\sigma$ range for 80% of the cells that are updated with data.

The model-based OSSE shows that the sparse nature of the surface pCO_2 data makes local slope estimates sensitive to the effects of subsampling interannual variability. The MCMC inversion is capable of imposing a model-based estimate of the interannual variability and compensating for much of the bias in local slope estimates. However, the MCMC result relies on having a decent prior estimate of the slope parameter and the interannual variability that will be imposed. In this demonstration, the imposed seasonal and interannual variability came from the true modeled case and the prior estimate of slope came from a similar class of models. Thus, this demonstration may be advantaged compared to the application of the method to real data, despite the error added to the synthetic observations, and may be thought of as offering a performance ceiling for interpretation of the MCMC results.

3. Results

We performed the inversion for all of the cells on the same grid used by *Takahashi et al.* [2009] to build the pCO_2 climatology. We chose to use the same grid for validation and comparison purposes. For each grid cell, the MCMC was initialized at the prior mean values for the parameter set (A,B,C,D) and the random walk was iterated for 50,000 steps. We excluded the first 10,000 steps to account for the burn-in of the random walk and allow the MCMC to move away from the prior means. To avoid biasing the samples of the posterior distribution with autocorrelation from the random walk, we use every tenth step in the random walk. This results in 4000 samples of the joint posterior distribution for (A, B, C, D). In this section, we show the resulting posterior distributions for the pCO_2 model parameters and the sensitivity studies to the IAV and SEAS terms.

3.1. MCMC Output

The global fit of the MCMC pCO_2 estimates to the measurements in LDEO2010 is comparable to what is found with linear regression. Supplement 1 shows the posterior estimate of pCO_2 alongside the data from LDEO2010 that was used to invert the model parameters for four random grid cells from each of the following regions: Polar Southern Ocean, Subpolar Southern Ocean, Equatorial Pacific, Subtropical and Subpolar North Pacific, and the Subpolar and Subtropical North Atlantic. The global mean residual of the pCO_2 estimates, against the LDEO2010 data, is −0.1 μatm and the root-mean-squared error is 16.8 μatm. We find that the empirical seasonality fits the observations better than the model-based seasonality and treat the empirical seasonality case as the standard inversion (see section 3.3 below). The results that are reported below are for the MCMC inversion featuring the empirical seasonality and the model-based interannual variability.

The prior and posterior distributions for the pCO_2 model parameters (A, B) are shown in Figure 3. The slope parameter *A* undergoes adjustments in many cells throughout the ocean, with particularly large regional changes in the North Pacific, North Atlantic, and Equatorial Pacific. These are the same places where the standard deviation of the prior is reduced by the inversion. The distribution of *B* also undergoes substantial changes, particularly in the Western Pacific and Subtropical North Atlantic. The uncertainty in the model parameter, *B*, is reduced throughout much of the ocean where LDEO2010 has observations. The prior and posterior time series in Figure 1a show that the MCMC inversion decreases the uncertainty and mean value of *A* and *B* in that cell. The slope parameter, *A*, has a prior mean estimate of 1.3 ± 0.5 μatm yr^{-1} and a posterior mean of 0.7 ± 0.2 μatm yr^{-1} and the intercept parameter *B* has a prior estimate of 350 ± 6 μatm and a posterior estimate 339 ± 2 μatm. Figure 1b shows the probability distribution function for the slope parameter *A* in that cell.

Figure 4 shows the posterior distributions of the scaling parameters *C* and *D*. The MCMC procedure scales the imposed signals to realize a better fit to the observations. The seasonal scaling, *C*, is decreased in the Equatorial Pacific and in the Southern Ocean and enhanced in some areas of the North Pacific. The global posterior mean value of *C* is 0.9 ± 0.5. The IAV term from MOM4p1-BLING is damped by the MCMC sampling though much of the globe. The global posterior mean value of *D* is 0.6 ± 0.8. The global damping of these two parameters indicates that there is substantial misfit from the data when they are imposed. Figure 1a provides an example of a region where the posterior seasonal cycle and interannual variability have been

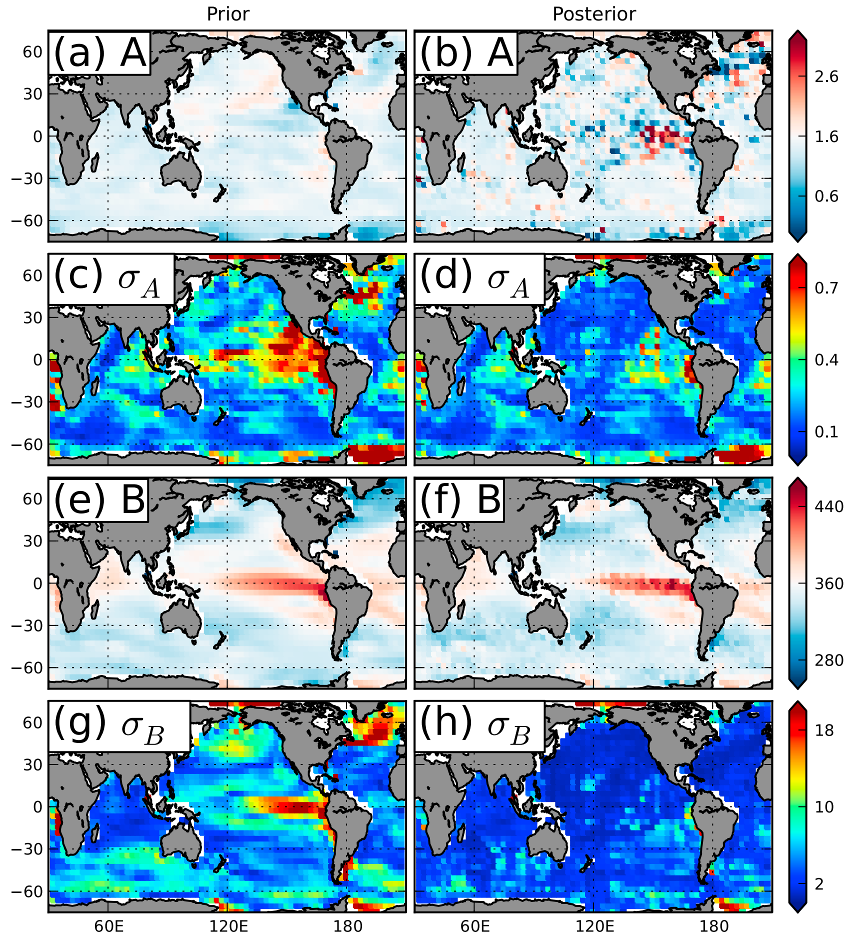

Figure 3. (a and b) The prior and posterior means and (c and d) standard deviations for the slope parameter, *A* in µatm, and (e–h) the intercept term, *B*, for the MCMC inversion of LDEO2010. The coloring in Figures 3a and 3b indicates growth with respect to the atmospheric growth rate in µatm yr^{-1} (blue indicates slower than atmospheric growth) and in Figures 3e and 3f indicates the June 1995 value with respect to the atmospheric pCO_2 (blue indicates ocean uptake of CO_2).

decreased such that the residuals from the pCO_2 time series is minimized. The posterior estimate for *C* is 0.8 ± 0.2 and the posterior value for *D* is 0.3 ± 0.2.

3.2. Flux Estimates

The patterns and magnitudes of the time mean fluxes calculated from the MCMC-based pCO_2 time series, Figure 5a, are comparable to the estimates of *Takahashi et al.* [2009]. The difference between the two is shown in Figure 5b. The MCMC pCO_2 results in higher ocean uptake of CO_2 in the Subpolar North Atlantic and over much of the Southern Ocean and increased outgassing in the Subpolar North Pacific. The regional

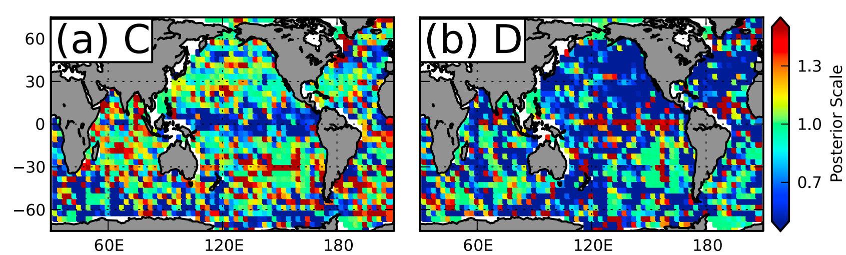

Figure 4. The posterior mean estimates for the scaling parameters (a) *C* and (b) *D* from the MCMC inversion of LDEO2010. Values smaller than 1 indicate that the amplitude of the imposed variability has been muted by the inversion.

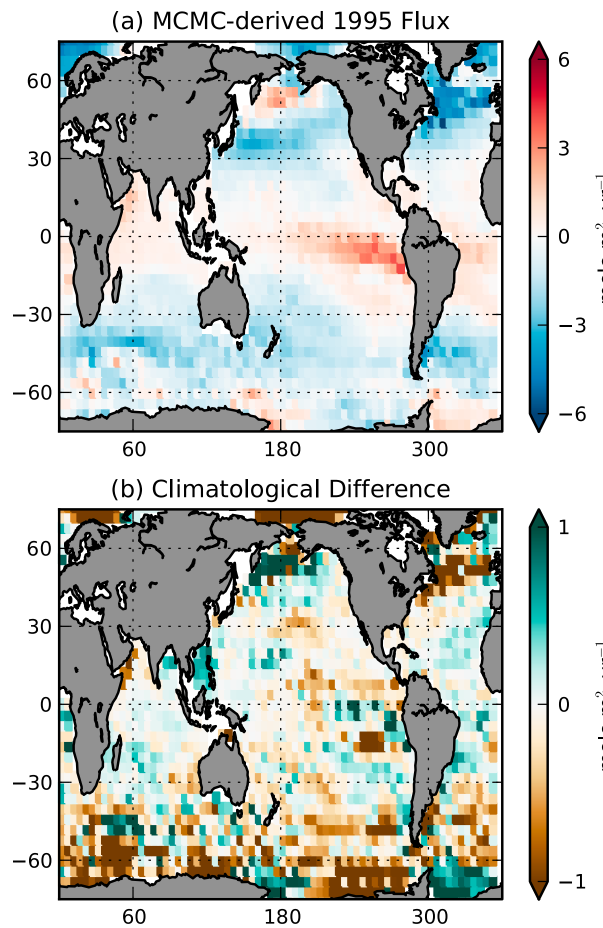

Figure 5. (a) The mean flux, 1995–2005, from the MCMC pCO_2 inversion is shown. (b) The difference between the MCMC-derived flux in Figure 5a and the climatology of *Takahashi et al.* [2009]. Positive values mean less uptake in the MCMC-derived estimates.

differences in the mean flux of CO_2 integrate to a difference in the global uptake of anthropogenic CO_2, as shown in Figure 6. This figure shows that in the decade centered on the year 2000, the mean MCMC estimate is higher than that of *Takahashi et al.* [2009] by approximately 0.2–0.3 PgC yr^{-1}. This difference is well within the $\pm 1\sigma$ uncertainty estimates from the two products and is principally due to the increased uptake in the Southern Ocean.

The time evolution of the MCMC fluxes is shown in Figure 6. There, we compare the evolving flux calculated using the MCMC inverted pCO_2 time series with a set of other estimates of anthropogenic CO_2 uptake, as compiled by *Gruber et al.* [2009]. The literature-based estimates of uptake show a generally increasing uptake by the ocean over this time period. Such an increase is consistent with the estimates from the MCMC implementations that make use of the empirical seasonality. The MCMC with interannual variability and empirical seasonality results in a global increase in the CO_2 uptake of 0.4 ± 0.1 PgC yr^{-1} decade^{-1}.

3.3. Sensitivity Studies

The sensitivity tests, where we exclude the interannual variability term and change the representation of the seasonal cycle, show cell-to-cell and regional differences in both the mean slope estimates and flux estimates but rather small impacts to the global totals. The supporting information include regional and global breakdowns of the sensitivity for each perturbation (Tables S3 and S4).

The sensitivity case designed to test the impact of including the IAV term on the pCO_2 inversion shows significant regional differences from the standard inversion, where IAV is excluded. Figure 7a shows the difference in the posterior slope estimate, *A*, between the standard case and the NOIAV case. We see that adding the interannual variability gives reduced posterior values of *A* in the Subtropical North Pacific, Western Equatorial Pacific, and in the Pacific and Indian sectors of the Southern Ocean. It also gives increasing values of *A* in the Eastern Equatorial Pacific, the Western Subpolar Atlantic, and the Southern Atlantic. The global difference is small, 0.0 ± 0.1 PgC yr^{-1}, though this is largely a result of compensating changes between regions (cf. Figure 7c). The global difference in the nominal year 2000 (1995–2005 average) flux is again small, with the IAV term decreasing the mean uptake by 0.017 ± 0.04 PgC yr^{-1}. The interannual variability in the NOIAV flux time series in Figure 6 comes from interannual variability in the atmospheric pCO_2 values.

The sensitivity of the inversion results to the representation of the seasonal cycle is larger than that for interannual variability, for both the posterior values of *A* and the decadal-mean flux about the year 2000 (cf. Figures 7b and 7d). Using the empirical seasonality instead of the model-based estimate maintains the global mean value of *A*. The global difference is 0.0 ± 0.3 μatm yr^{-1}, though there are particularly large decreases in the posterior value of *A* in the Atlantic and Equatorial Pacific. These decreases are partially compensated by increases in the value of *A* in the North Pacific. The flux is significantly altered in the North Atlantic and the Southern Ocean, with both regions showing reduced uptake under the empirical seasonal

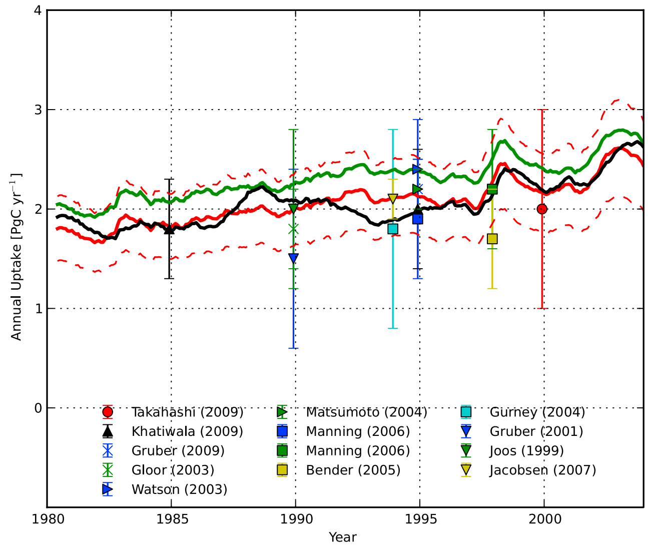

Figure 6. The total uptake of anthropogenic CO_2 time series, 1980–2009, for the MCMC featuring the MOM4p1-BLING seasonal cycle (green) and the empirical seasonal cycle (red) and the MCMC version with the MOM4p1-BLING seasonal cycle and no interannual variability (black). The dotted lines indicate $\pm$ 1 σ for the global integral, including the uncertainty in gas exchange piston velocity. The red dot and associated error bars represent the anthropogenic uptake calculated by *Takahashi et al.* [2009] of 2.0 $\pm$ 1.0 PgC yr^{-1}. The black triangles show the decadally averaged estimates from *Khatiwala et al.* [2009]. The other box and whisker plots indicate other estimates for anthropogenic CO_2 uptake by the ocean from Table 1 in *Gruber et al.* [2009].

cycle. The global difference in the nominal flux is a decreased uptake of 0.2 $\pm$ 0.05 PgC yr^{-1}. The flux time series in Figure 6 shows the combined results of the differences in the mean flux and the evolution of the surface pCO_2. The fluxes calculated from the inversion with the MOM4p1-BLING seasonality show larger uptake than the other inversion cases but also show less increase in CO_2 uptake of the ocean through time.

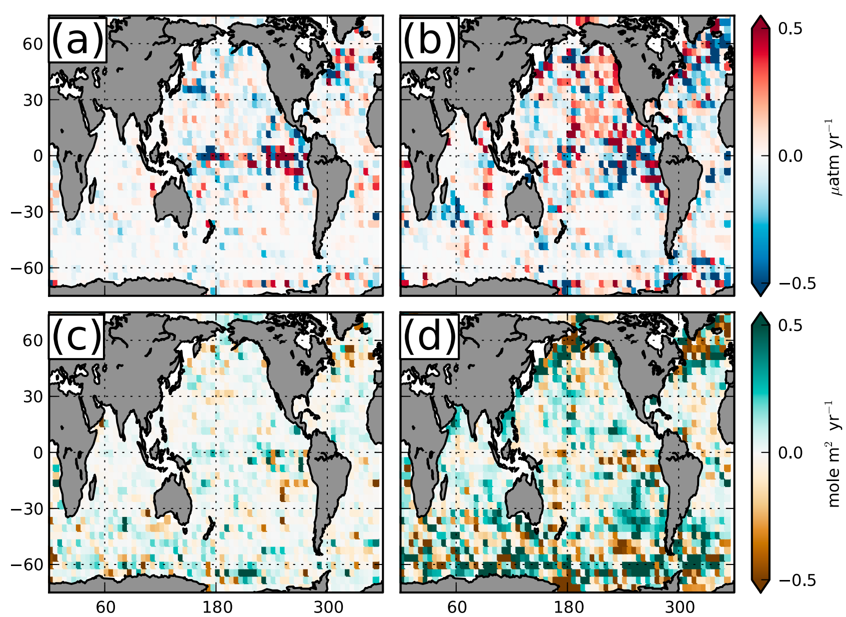

Figure 7. (a) The difference in the mean of *A* between the standard MCMC inversion and the run with no interannual variability and (b) the same between the standard case and the run with the MOM4p1-BLING based seasonality. In both panels, positive values indicate faster growth in the standard case. (c) The difference in mean year 2000 flux between the standard and no interannual variability cases and (d) the same for the seasonal difference. Here positive values indicate more outgassing or less uptake.

10.1002/2013GB004585

4. Discussion

In the following subsections, we discuss the results of the MCMC-based inversion of surface pCO_2 in light of previous studies. We show how this global analysis is consistent with the results of previous regional analyses of pCO_2. This is an important check, as much of the data that was used in these previous studies is included in LDEO2010. The section ends with an analysis of the Southern Ocean pCO_2 trend, where our trend differs significantly from recently published results.

As a matter of terminology, in this section, we often refer to the significance of the posterior trend estimate, *A*. We refer to the trend as significantly "lagging" the atmosphere when the 90th percentile of the posterior distribution for *A* is less than the atmospheric growth rate of 1.6 µatm yr^{-1}. The trend is significantly "leading" the atmosphere with the 10th percentile of the posterior distribution for *A* is greater than the atmospheric growth rate. When results are referred to as not significant, though the mean estimate may be different from 1.6 µatm yr^{-1}, it means that the value of *A* is cannot be separated from the atmospheric increase at the 10% certainty level in our one-sided test. A surface pCO_2 trend that lags the atmosphere tends toward more uptake of CO_2 by the ocean and a trend that leads the atmosphere tends toward less uptake.

The MCMC estimates a global mean increase in surface ocean pCO_2 of 1.4 ± 0.5 µatm yr^{-1}. The posterior mean value of *A* is less than the atmospheric growth rate for 73% of the ocean surface. The difference from the atmospheric value is significant for 42% of the ocean surface, with 34% lagging and 8% leading the atmospheric growth rate. Regionally, we see a significant lagging of the atmospheric pCO_2 through much of the North Pacific, the Subpolar North Atlantic, and parts of the Southern Ocean. We calculate a surface pCO_2 growth faster than the atmosphere in parts of the Eastern Equatorial Pacific, Subtropical North Atlantic, and Southern Ocean.

For comparison of the time evolution of the fluxes, which is closely related to the time evolution of surface pCO_2, the inverse estimate of *Khatiwala et al.* [2009] shows an increase of 0.5 PgC yr^{-1} $decade^{-1}$ from the 1980s (1.8 ± 0.5) to the 2000s (2.3 ± 0.6), similar to the growth rate that we find, 0.4 ± 0.1 PgC yr^{-1} $decade^{-1}$. The other estimates of the global ocean CO_2 uptake seem consistent with the decadal increases in the MCMC-derived oceanic uptake (cf. Figure 6).

4.1. Pacific

In the MCMC result, the Northern Subtropical Pacific shows a slower than atmospheric growth in the surface pCO_2, in agreement with *Takahashi et al.* [2006]. The average slope in the region is 1.5 ± 0.4 µatm yr^{-1} with a small standard error, cf. Table 3, which indicates a coherent behavior in the basin. We find that many cells in this regions significantly lag the atmosphere, indicating that the MCMC-derived pCO_2 is estimating a growing flux. The whole North Pacific shows a total increased uptake greater than 0.25 PgC yr^{-1} over the whole period, see Table S2 (supporting information).

In the Eastern Equatorial Pacific, we found oceanic pCO_2 increasing faster than the atmosphere in the region of upwelling, with a slower than atmospheric growth north of the upwelling. These trends are consistent with the analysis of *Feely et al.* [2006]. In the Western Equatorial Pacific, we see a trend toward increasing ocean uptake as in *Ishii et al.* [2004]. The whole Equatorial Pacific is characterized by strong mean trends (cf. Figure 3b), but the uncertainty in the estimates is too large for the slope to be significantly different from the atmospheric one (cf. Figure 3b). The high level of uncertainty in the cell-by-cell estimates leads to substantial uncertainty in the mean trends for the region, cf. Table 3.

4.2. Atlantic

In the MCMC estimate, the subtropical gyre region of the North Atlantic has a regional average trend parameter of 1.6 ± 0.4 µatm yr^{-1} (cf. Table 3). Figure 3b shows that the eastern subtropical gyre has a region of faster than atmospheric growth, which has been identified previously [*Schuster and Watson*, 2007]. A slower than atmospheric growth in the western part of the gyre compensates for the faster than atmospheric growth in our result. Thus, our estimate of the regional average is not significantly different from the atmospheric growth rate because we average over strong lagging and leading signals.

Of note in both the Subtropical and Subpolar North Atlantic is the basin-averaged consistency with the recent results of *McKinley et al.* [2011]. They were the first to show that the regional trends in the North Atlantic were strongly influenced by the time window over which they were reported. They showed that

Table 3. $p\mathrm{CO_2}$ Slope Estimates[a]

Region	CT Regions[b]	Area (%)	MCMC Slope (μatm $\mathrm{yr^{-1}}$) (SE)
World	All	100.0	1.4 ± 0.6 (0.0)
North Pacific	10-16	12.3	1.4 ± 0.4 (0.0)
Eastern Equatorial Pacific	19	4.8	1.6 ± 0.7 (0.1)
Subpolar North Atlantic	2,3	4.8	1.3 ± 0.5 (0.1)
Subtropical North Atlantic	4	3.9	1.6 ± 0.4 (0.1)
Southern Ocean (<45°S)	9,10,25,30	17.3	1.4 ± 0.5 (0.0)

[a]Regionally averaged $p\mathrm{CO_2}$ slopes with uncertainty listed from both the sum of squares and the standard error for the region.
[b]Regions from CARBONTRACKER, http://www.esrl.noaa.gov/gmd/ccgg/carbontracker/index.html.

trends in the surface $p\mathrm{CO_2}$ became indistinguishable from the atmospheric growth rate for time series approaching 30 years. This is true in our estimates of the North Atlantic growth rates as well. While our result shows that within each region, there are cells with significantly different growth rates than the atmosphere, that significant difference is lost in regional averaging.

4.3. Southern Ocean

The most notable difference between our results and previous studies is in the Southern Ocean (< 45°S) where we show a slower than atmospheric growth in the mean, 1.4 ± 0.5 μatm $\mathrm{yr^{-1}}$, but not a significant difference from the atmosphere. This result differs from that of *Lenton et al.* [2012], who showed an increasing trend of 2.2 ± 0.2μatm $\mathrm{yr^{-1}}$ for the period 1995–2008 using ordinary least squares fitting of the measurements in LDEO2010. We can examine the reasons for the disparity by sampling the $p\mathrm{CO_2}$ time series generated by the MCMC inversion and using ordinary least squares fitting to calculate the $p\mathrm{CO_2}$ trends for the whole region as in [*Lenton et al.*, 2012]. To evaluate the influence of the seasonal cycle and interannual variability, we then apply corrections to the sampled MCMC fields from the SEAS and IAV time series and recalculate the trend.

Table 4 shows the slope estimates that result from estimating the $p\mathrm{CO_2}$ trends with the MCMC output, in the manner laid out in section 2.5, for the full period, 1980–2009, and the shorter period, 1995–2008, where LDEO2010 has values. The slope estimates calculated directly from the MCMC $p\mathrm{CO_2}$ output, sampled where observations exist in LDEO2010, show a faster than atmospheric growth rate, consistent with the one from *Lenton et al.* [2012]. The table shows that including seasonal and interannual adjustments from the IAV and SEAS terms brings the basin slope estimates closer to the MCMC-based estimate of 1.4 ± 0.5 μatm $\mathrm{yr^{-1}}$. In this case, including the seasonal cycle plays a larger role than the interannual variability, but both decrease the slope estimate in the 1995–2008 time period.

The role of the SEAS and IAV adjustments is lessened by taking the whole period into account, which is shown in the second row of Table 4. As more samples are included, covering a wider time window, the calculated trends come to resemble the mean behavior of the MCMC-based $p\mathrm{CO_2}$ history. This result is consistent with the study of *Fay and McKinley* [2013] where the authors show that the multidecadal trend in the Southern Ocean $p\mathrm{CO_2}$ is slower but statistically indistinguishable from that in the atmosphere and that trends calculated from shorter time periods can vary substantially, compared to the atmospheric trend, under decadal variability.

Table 4. Alternative $p\mathrm{CO_2}$ Estimates[a]

Dates	A^{*}_{sub}	A_{sub}	$A_{sub} + A_{iav}$
07/1995 to 06/2008	2.23 ± 0.31	1.50 ± 0.18	1.45 ± 0.19
01/1980 to 12/2009	1.87 ± 0.09	1.68 ± 0.05	1.64 ± 0.06

[a]The slope calculated by sampling the MCMC output without adjustments A_{sub*}, with seasonal adjustments A_{sub}, and with seasonal and interannual adjustments (IAV) at LDEO2010 points within two time windows.

In order to better understand the $p\mathrm{CO_2}$ trend in the Southern Ocean, we separated the MCMC-derived $p\mathrm{CO_2}$ into temperature- and nontemperature-driven components [*McKinley et al.*, 2006] and calculated the trend in each component from 1980 to 2005 using the monthly values and ordinary

10.1002/2013GB004585

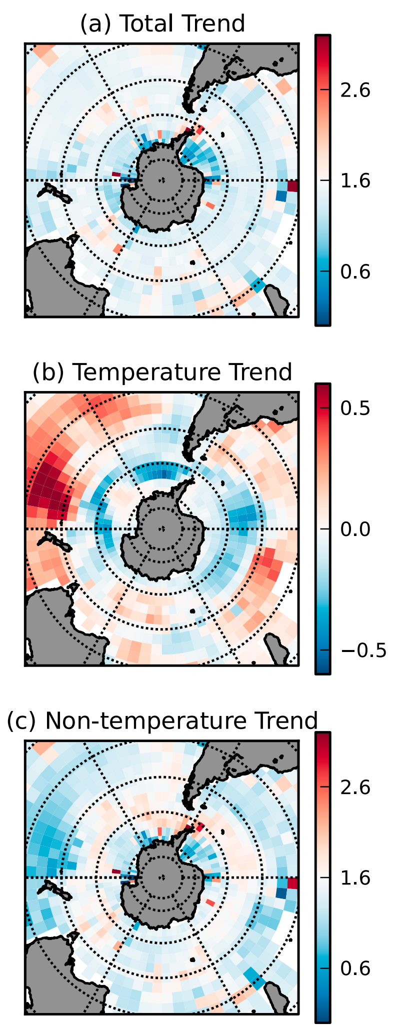

Figure 8. (a) The MCMC slope estimate for the Southern Ocean in μatm yr^{-1}. (b) The trend in the temperature-driven component of $p\text{CO}_2$ and (c) the nontemperature component trend.

least squares methods. For the temperature record, we used the NOAA monthly sea surface temperature (SST) optimal interpolation product NOAA-OI.v2 [*Reynolds et al.*, 2002]. This SST product shows a cooling trend in the surface temperatures south of 45°S for the 1980–2005 period. That negative trend in temperature drives a negative trend in the temperature-driven $p\text{CO}_2$, as in Figure 8b. A qualitatively similar surface cooling is expressed in the Hadley Center SST product HadISST1 [*Rayner et al.*, 2003], the temperature measurements made coincidentally with the $p\text{CO}_2$ samples [*Fay and McKinley*, 2013], and in analyses based on float data (albeit for a shorter period) [*Gille*, 2008]. The negative trend in surface $p\text{CO}_2$ masks a trend in the chemically driven $p\text{CO}_2$, shown in Figure 8c, which is faster than the atmospheric growth for much of the ocean between 50°S and 65°S, in the region of the Antarctic Circumpolar Current (ACC). The faster than atmospheric growth is strongest in the Drake Passage and the Southern Atlantic Oceans. The zonal means of the component trends for the Southern Ocean are shown in Table 5 where it can be seen that the trend in temperature component moderates a faster than atmospheric growth in the chemical component between 50°S and 62°S.

The balance between the temperature- and nontemperature-driven variations in surface $p\text{CO}_2$ in the Southern Ocean points to an interesting set of dynamics, relating to the response of the carbon fluxes in the Southern Ocean to changes in climate and the proposed feedbacks to changes in wind stress [*Le Quéré et al.*, 2007]. Over the 1980–2010 period, reanalysis products show a significant increase in the Southern Annular Mode (SAM) index and an intensification of the westerly winds [*Swart and Fyfe*, 2012]. Surface cooling in the Southern Ocean has previously been associated with positive phases of the SAM index, with the intensification and poleward shift of the westerlies and increased Ekman flow and sea-air interaction playing a significant role in that cooling [*Verdy et al.*, 2006; *Ciasto and Thompson*, 2008]. Likewise, previous modeling studies of the Southern Ocean have proposed that positive deviations of the SAM index can drive enhanced northward transport and upwelling of carbon-rich deep water via increases in Ekman flow and the associated meridional overturning [*Treguier et al.*, 2010].

The results of the MCMC $p\text{CO}_2$ inversion seem to be consistent with the model-based process studies of carbon flux, where the circulation-driven $p\text{CO}_2$ has increased in the surface Southern Ocean as the SAM index has increased over the last 30 years, resulting from the net effect of upwelling of carbon-rich waters that is not fully compensated by increasing biological production [*Lovenduski et al.*, 2008]. We find that this increase was counteracted by a cooling of the surface temperatures, possibly due to the same circulation processes, such that the total outgassing from the Southern Ocean actually reduced, i.e., the uptake of anthropogenic CO_2 increased. How these processes will continue to respond to the projected changes in the annual mean and seasonal SAM indices [*Polvani et al.*, 2011] is an open area of research, particularly as some high-resolution modeling studies indicate that permanent changes in the SAM index might drive long-term warming of the Southern Ocean SST as eddy heat fluxes compensate for the increased Ekman flow [*Hogg et al.*, 2008; *Screen et al.*, 2009]. Forthcoming modeling studies with high-resolution models aim to address

Table 5. pCO_2 Component Trends[a]

Latitude	Total	Temperature	Nontemperature
44.0	0.13 ± 0.15	0.06 ± 0.17	0.18 ± 0.27
48.0	0.10 ± 0.16	-0.01 ± 0.15	0.09 ± 0.21
52.0	0.07 ± 0.18	-0.09 ± 0.12	-0.02 ± 0.17
56.0	0.14 ± 0.12	-0.13 ± 0.14	-0.00 ± 0.18
60.0	0.15 ± 0.24	-0.16 ± 0.13	-0.03 ± 0.27
64.0	0.28 ± 0.40	-0.14 ± 0.14	0.09 ± 0.40
68.0	0.36 ± 0.50	-0.03 ± 0.06	0.26 ± 0.48
72.0	0.75 ± 0.46	-0.00 ± 0.03	0.67 ± 0.44

[a]The zonally averaged trend in surface pCO_2 μatm yr^{-1} and the temperature and nontemperature components thereof for the Southern Ocean. The total and nonthermal pCO_2 trends are shown as deviations from the atmospheric growth rate. The uncertainty listed here is the zonal sample standard deviation of the mean trend and conveys the level of zonal discord in the calculated surface trend.

how the carbon system responds to changes in SAM at the process level.

5. Conclusions

In this paper, we present the application of MCMC sampling to the estimation of long-term trends in surface pCO_2 and air-sea CO_2 fluxes based on surface pCO_2 data and model-based variability. This method allows us to formally introduce modeled interannual and seasonal variability to the trend estimation problem and reduce biases that result from the sparse nature of our observations of ocean carbon. The results can be thought of as a plausible time history of surface pCO_2, and its trends, that is constrained to data where it is available and otherwise model based. The model-based variability incorporates the effects of ocean circulation, biogeochemistry, and air-sea interaction on surface pCO_2 as represented by an ocean general circulation model is that forced by atmospheric reanalysis. Thus, this is a first step toward estimating surface pCO_2 history while incorporating process-based constraints.

The mean flux estimates generated by the MCMC method are broadly consistent with the canonical estimates of *Takahashi et al.* [2009] and other studies based on ocean inversion. For global trends, we found that the ocean exhibits an increasing uptake of CO_2 over the time period 1980–2009, consistent with a global surface pCO_2 that is growing more slowly than the atmospheric value. The MCMC with interannual variability and empirical seasonality results in a global increase in the CO_2 uptake of 0.4 ± 0.1 PgC yr^{-1} $decade^{-1}$. This would account for nearly 50% of the global carbon sink increase calculated by *Ballantyne et al.* [2012].

Some regions show pCO_2 trends that are notably different from the global average. The subtropical North Atlantic and Equatorial Pacific are the two regions that show the fastest growth in surface pCO_2, indicating a decreasing uptake of carbon by the ocean. Some parts of the Southern Ocean also show faster than atmospheric growth in the surface pCO_2, but the region as a whole (south of 45°S) is an increasing sink. Interestingly, our results indicate that dissolved inorganic carbon (DIC) is increasing throughout the Southern Ocean, but that surface cooling trends are more than compensating for the growth in DIC such that a slower than atmospheric pCO_2 growth rate and increasing uptake are maintained.

We note that these are regions of high seasonal and interannual variability and that detecting secular trends against the background variations will remain a challenge in the future. Including interannual variability via the MCMC method has a notable effect on local trend estimates and is an important consideration for studies of surface pCO_2, although we found that the effect tended to be smaller when taking regional averages and calculating global trends in the air-sea CO_2 flux.

Proper representation of the seasonal cycle around the global ocean remains a priority. Different estimates of the seasonal cycle lead to substantial differences in the MCMC-based estimates of local and regional pCO_2 trends and mean fluxes. Ultimately, the sensitivity to the seasonal cycle drives significant differences in the global CO_2 fluxes. Based on this sensitivity, improved observations and models of the seasonal cycle in surface pCO_2 are a necessity for improving carbon flux estimates based on surface observations and for providing additional constraints on the seasonal variations in surface pCO_2.

The MCMC technique that we present is a promising method for continued investigation of the historical pCO_2. Possible extensions of this work might use the flexibility of the MCMC method to include other types of observation-driven data to improve the pCO_2 estimation. For example, SST observations and ocean color data might help to resolve the seasonal cycle in pCO_2. Likewise, allowing the grid structure to be refined by the MCMC where there is sufficient information in the pCO_2 data would benefit the regional veracity of the resulting pCO_2 history and could take advantage of the improved spatial and temporal resolution in updating global databases of surface pCO_2 measurements, such as SOCAT [*Pfeil et al.*, 2012].

Acknowledgments
This work benefitted from the help of several draft readers: N. Gruber, M. Gloor, D. Medvigy, A. Jacobsen, and two reviewers with insightful comments. We thank R. Slater for assistance with managing model simulations. J.D.M. and J.L.S. were supported by NOAA-NA11OAR4310066 during the performance of this work. The contribution of K.R. comes through awards NA17RJ2612 and NA080AR4320752, which includes support through the NOAA Office of Climate Observations (OCO). The statements, findings, conclusions, and recommendations are those of the authors and do not necessarily reflect the views of NOAA or the U.S. Department of Commerce. The data used within this paper is freely available via the U.S. Oak Ridge National Laboratory Carbon Dioxide Information Analysis Center.

References

Aumont, O., and L. Bopp (2006), Globalizing results from ocean in situ iron fertilization studies, *Global Biogeochem. Cycles*, *20*, GB2017, doi:10.1029/2005GB002591.

Ballantyne, A., C. Alden, J. Miller, P. Tans, and J. White (2012), Increase in observed net carbon dioxide uptake by land and oceans during the past 50 years, *Nature*, *488*, 70–72.

Bates, N. R. (2007), Interannual variability of the oceanic CO_2 sink in the subtropical gyre of the North Atlantic Ocean over the last 2 decades, *J. Geophys. Res.*, *112*, C09013, doi:10.1029/2006JC003759.

Bellouin, N., et al. (2011), The HadGem2 family of Met Office Unified model climate configurations, *Geosci. Model Dev. Discuss.*, *4*, 765–841.

Bender, M. L., D. T. Ho, M. B. Hendricks, R. Mika, M. O. Battle, P. P. Tans, T. J. Conway, B. Sturtevant, and N. Cassar (2005), Atmospheric O_2/N_2 changes, 1993–2002: Implications for the partitioning of fossil fuel CO_2 sequestration, *Global Biogeochem. Cycles*, *19*, GB4017, doi:10.1029/2004GB002410.

Brodeau, L., B. Barnier, A.-M. Treguier, T. Penduff, and S. Gulev (2010), An ERA40-based atmospheric forcing for global ocean circulation models, *Ocean Model.*, *31*, 88–104.

Ciasto, L. M., and D. W. Thompson (2008), Observations of large-scale ocean-atmosphere interaction in the Southern Hemisphere, *J. Clim.*, *21*, 1244–1259.

Doney, S. C., B. Tilbrook, S. Roy, N. Metzl, C. Le Quéré, M. Hood, R. A. Feely, and D. Bakker (2009a), Surface-ocean CO_2 variability and vulnerability, *Deep Sea Res. Part II*, *56*, 504–511.

Doney, S. C., I. Lima, R. A. Feely, D. M. Glover, K. Lindsay, N. Mahowald, J. K. Moore, and R. Wanninkhof (2009b), Mechanisms governing interannual variability in upper-ocean inorganic carbon system and air–sea CO_2 fluxes: Physical climate and atmospheric dust, *Deep Sea Res. Part II*, *56*, 640–655.

Dore, J. E., R. Lukas, D. W. Sadler, M. J. Church, and D. M. Karl (2009), Physical and biogeochemical modulation of ocean acidification in the central North Pacific, *Proc. Natl. Acad. Sci.*, *106*, 12,235–12,240.

Dunne, J. P., et al. (2012), GFDL's ESM2 global coupled climate-carbon Earth System Models. Part I: Physical formulation and baseline simulation characteristics, *J. Clim.*, *25*, 6646–6665.

Dunne, J. P., et al. (2013), GFDL's ESM2 global coupled climate-carbon Earth system models. Part II: Carbon system formulation and baseline simulation characteristics, *J. Clim.*, *26*, 2247–2267.

Fay, A. R., and G. A. McKinley (2013), Global trends in surface ocean pCO_2 from in situ data, *Global Biogeochem. Cycles*, *27*, 541–557, doi:10.1002/gbc.20051.

Feely, R., T. Takahashi, R. Wanninkhof, M. McPhaden, C. Cosca, S. Sutherland, and M.-E. Carr (2006), Decadal variability of the air-sea CO_2 fluxes in the equatorial Pacific Ocean, *J. Geophys. Res.*, *111*, C08S90, doi:10.1029/2005JC003129.

Friedlingstein, P., et al. (2006), Climate-carbon cycle feedback analysis: Results from the C^4MIP model intercomparison, *J. Clim.*, *19*, 3337–3353.

Galbraith, E. D., et al. (2011), Climate variability and radiocarbon in the CM2Mc Earth system model, *J. Clim.*, *24*, 4230–4254.

Gille, S. T. (2008), Decadal-scale temperature trends in the Southern Hemisphere Ocean, *J. Clim.*, *21*, 4749–4765.

Gloor, M., N. Gruber, J. Sarmiento, C. Sabine, R. Feely, and C. Rödenbeck (2003), A first estimate of present and preindustrial air-sea CO_2 flux patterns based on ocean interior carbon measurements and models, *Geophys. Res. Lett.*, *30*(1), 1010, doi:10.1029/2002GL015594.

Griffies, S. M., M. J. Harrison, R. C. Pacanowski, and A. Rosati (2004), *A technical guide to MOM4, Tech. Rep.*, NOAA GFDL, Princeton, N. J.

Gruber, N., and C. D. Keeling (2001), An improved estimate of the isotopic air-sea disequilibrium of CO_2: Implications for the oceanic uptake of anthropogenic CO_2, *Geophys. Res. Lett.*, *28*(3), 555–558.

Gruber, N., et al. (2009), Oceanic sources, sinks, and transport of atmospheric CO_2, *Global Biogeochem. Cycles*, *23*(1), GB1005, doi:10.1029/2008GB003349.

Gurney, K. R., et al. (2004), Transcom 3 inversion intercomparison: Model mean results for the estimation of seasonal carbon sources and sinks, *Global Biogeochem. Cycles*, *18*(1), GB1010, doi:10.1029/2003GB002111.

Hastings, W. K. (1970), Monte Carlo sampling methods using Markov chains and their applications, *Biometrika*, *57*(1), 97–109.

Hogg, A. M. C., M. P. Meredith, J. R. Blundell, and C. Wilson (2008), Eddy heat flux in the Southern Ocean: Response to variable wind forcing, *J. Clim.*, *21*(4), 608–620.

Hurrell, J. W., J. J. Hack, D. Shea, J. M. Caron, and J. Rosinski (2008), A new sea surface temperature and sea ice boundary dataset for the community atmosphere model, *J. Clim.*, *21*(19), 5145–5153.

Ishii, M., S. Saito, T. Tokieda, T. Kawano, K. Matsumoto, and H. Y. Inoue (2004), Variability of surface layer CO_2 parameters in the western and central Equatorial Pacific, in *Global Environmental Changes in the Ocean and on Land*, edited by M. Shiyomi et al., pp. 59–94, TERRAPUB, Tokyo.

Jacobson, A. R., S. E. M. Fletcher, N. Gruber, J. L. Sarmiento, and M. Gloor (2007), A joint atmosphere-ocean inversion for surface fluxes of carbon dioxide: 2. Regional results, *Global Biogeochem. Cycles*, *21*(1), GB1020, doi:10.1029/2006GB002703.

Joos, F., R. Meyer, M. Bruno, and M. Leuenberger (1999), The variability in the carbon sinks as reconstructed for the last 1000 years, *Geophys. Res. Lett.*, *26*(10), 1437–1440.

Kalnay, E., et al. (1996), The NCEP/NCAR 40-year reanalysis project, *Bull. Am. Meteorol. Soc.*, *77*(3), 437–471.

Keeling, C. D., S. C. Piper, R. B. Bacastow, M. Wahlen, T. P. Whorf, M. Heimann, and H. A. Meijer (2001), Exchanges of atmospheric CO_2 and $^{13}CO_2$ with the terrestrial biosphere and oceans from 1978 to 2000. I. Global aspects, *Tech. Rep.*, Scripps Institute of Oceanography, UC San Diego, Calif.

Khatiwala, S., F. Primeau, and T. Hall (2009), Reconstruction of the history of anthropogenic CO_2 concentrations in the ocean, *Nature*, *462*(7271), 346–349.

Large, W., and S. Yeager (2009), The global climatology of an interannually varying air–sea flux data set, *Clim. Dyn.*, *33*(2-3), 341–364.

Le Quéré, C., et al. (2007), Saturation of the Southern Ocean CO_2 sink due to recent climate change, *Science*, *316*(5832), 1735–1738.

Le Quéré, C., T. Takahashi, E. T. Buitenhuis, C. Rödenbeck, and S. C. Sutherland (2010), Impact of climate change and variability on the global oceanic sink of CO_2, *Global Biogeochem. Cycles*, *24*(4), GB4007, doi:10.1029/2009GB003599.

Lenton, A., R. J. Matear, and B. Tilbrook (2006), Design of an observational strategy for quantifying the Southern Ocean uptake of CO_2, *Global Biogeochem. Cycles*, *20*(4), GB4010, doi:10.1029/2005GB002620.

Lenton, A., N. Metzl, T. Takahashi, M. Kuchinke, R. J. Matear, T. Roy, S. C. Sutherland, C. Sweeney, and B. Tilbrook (2012), The observed evolution of oceanic pCO_2 and its drivers over the last two decades, *Global Biogeochem. Cycles*, *26*(2), GB2021, doi:10.1029/2011GB004095.

Lovenduski, N. S., N. Gruber, and S. C. Doney (2008), Toward a mechanistic understanding of the decadal trends in the Southern Ocean carbon sink, *Global Biogeochem. Cycles*, *22*(3), GB3016, doi:10.1029/2007GB003139.

Manning, A. C., and R. F. Keeling (2006), Global oceanic and land biotic carbon sinks from the Scripps atmospheric oxygen flask sampling network, *Tellus B*, *58*(2), 95–116.

Matsumoto, K., et al. (2004), Evaluation of ocean carbon cycle models with data-based metrics, *Geophys. Res. Lett.*, *31*(7), L07303, doi:10.1029/2003GL018970.

McKinley, G., T. Takahashi, E. Buitenhuis, F. Chai, J. Christian, S. Doney, M. Jiang, K. Lindsay, J. Moore, and C. Le Quéré (2006), North Pacific carbon cycle response to climate variability on seasonal to decadal timescales, *J. Geophys. Res.*, *111*(C7), C07S06, doi:10.1029/2005JC003173.

McKinley, G. A., A. R. Fay, T. Takahashi, and N. Metzl (2011), Convergence of atmospheric and North Atlantic carbon dioxide trends on multidecadal timescales, *Nat. Geosci.*, *4*(9), 606–610.

Pfeil, B., et al. (2012), A uniform, quality controlled Surface Ocean CO_2 Atlas (SOCAT), *Earth Syst. Sci. Data Discuss*, *5*(2), 735–780, eSSDD.

Polvani, L. M., M. Previdi, and C. Deser (2011), Large cancellation, due to ozone recovery, of future Southern Hemisphere atmospheric circulation trends, *Geophys. Res. Lett.*, *38*(4), L04707, doi:10.1029/2011GL046712.

Rayner, N., D. Parker, E. Horton, C. Folland, L. Alexander, D. Rowell, E. Kent, and A. Kaplan (2003), Global analyses of sea surface temperature, sea ice, and night marine air temperature since the late nineteenth century, *J. Geophys. Res.*, *4407*(D14), doi:10.1029/2002JD002670.

Reynolds, R. W., N. A. Rayner, T. M. Smith, D. C. Stokes, and W. Wang (2002), An improved in situ and satellite SST analysis for climate, *J. Clim.*, *15*(13), 1609–1625.

Rodgers, K., A. Aumont, S. Mikaloff-Fletcher, Y. Plancherel, L. Bopp, C. de Boyer Montégut, D. Iudicone, R. Keeling, G. Madec, and R. Wanninkof (2013), Strong sensitivity of Southern Ocean carbon uptake and nutrient cycling to wind stirring, *Biogeosci. Discuss.*, *10*(9), 15,033–15,076, doi:10.5194/bgd-10-15033-2013.

Sabine, C., et al. (2012), Surface Ocean CO_2 Atlas (SOCAT) gridded data products, *Earth Syst. Sci. Data Discuss.*, *5*(2), 781–804.

Sarmiento, J., M. Gloor, N. Gruber, C. Beaulieu, A. Jacobson, S. Mikaloff Fletcher, S. Pacala, and K. Rodgers (2010), Trends and regional distributions of land and ocean carbon sinks, *Biogeosciences*, *7*(8), 2351–2367.

Schmidt, G. A., et al. (2006), Present-day atmospheric simulations using GISS ModelE: Comparison to in situ, satellite, and reanalysis data, *J. Clim.*, *19*(2), 153–192.

Schuster, U., and A. J. Watson (2007), A variable and decreasing sink for atmospheric CO_2 in the North Atlantic, *J. Geophys. Res.*, *112*(C11), C11006, doi:10.1029/2006JC003941.

Screen, J. A., N. P. Gillett, D. P. Stevens, G. J. Marshall, and H. K. Roscoe (2009), The role of eddies in the Southern Ocean temperature response to the southern annular mode, *J. Clim.*, *22*(3), 806–818.

Swart, N., and J. Fyfe (2012), Observed and simulated changes in the Southern Hemisphere surface westerly wind-stress, *Geophys. Res. Lett.*, *39*(16), L16711, doi:10.1029/2012GL052810.

Sweeney, C., E. Gloor, A. R. Jacobson, R. M. Key, G. McKinley, J. L. Sarmiento, and R. Wanninkhof (2007), Constraining global air-sea gas exchange for CO_2 with recent bomb ^{14}C measurements, *Global Biogeochem. Cycles*, *21*(2), GB2015, doi:10.1029/2006GB002784.

Takahashi, T., S. C. Sutherland, R. A. Feely, and R. Wanninkhof (2006), Decadal change of the surface water pCO_2 in the North Pacific: A synthesis of 35 years of observations, *J. Geophys. Res.*, *111*(C7), C07S05, doi:10.1029/2005JC003074.

Takahashi, T., et al. (2009), Climatological mean and decadal change in surface ocean pCO_2, and net sea–air CO_2 flux over the global oceans, *Deep Sea Res. Part II*, *56*(8), 554–577.

Takahashi, T., S. Sutherland, and A. Kozyr (2012), Global ocean surface water partial pressure of CO_2 database: Measurements performed during 1957–2011 (version 2011), *ORNL/CDIAC-160*, NDP-088(V2011), Carbon Dioxide Information Analysis Center, Oak Ridge National Laboratory, U.S. Department of Energy, Oak Ridge, Tennessee.

Treguier, A. M., J. Le Sommer, J.-M. Molines, and B. De Cuevas (2010), Response of the Southern Ocean to the southern annular mode: Interannual variability and multidecadal trend, *J. Phys. Oceanogr.*, *40*(7), 1659–1668.

Uppala, S. M., et al. (2005), The ERA-40 re-analysis, *Q. J. R. Meteorolog. Soc.*, *131*(612), 2961–3012.

Verdy, A., J. Marshall, and A. Czaja (2006), Sea surface temperature variability along the path of the Antarctic circumpolar current, *J. Phys. Oceanogr.*, *36*(7), 1317–1331.

Wanninkhof, R., W. E. Asher, D. T. Ho, C. Sweeney, and W. R. McGillis (2009), Advances in quantifying air-sea gas exchange and environmental forcing*, *Mar. Sci.*, *1*, 213–244.

Wanninkhof, R., et al. (2013), Global ocean carbon uptake: Magnitude, variability and trends, *Biogeosciences*, *10*(3), 1983–2000, doi:10.5194/bg-10-1983-2013.

Watson, A. J., and J. C. Orr (2003), Carbon dioxide fluxes in the global ocean, in *Ocean Biogeochemistry*, edited by M. J. R. Fasham, pp. 123–143, Springer, Berlin Heidelberg.

Woloszyn, M., M. Mazloff, and T. Ito (2011), Testing an eddy-permitting model of the Southern Ocean carbon cycle against observations, *Ocean Model.*, *39*(1), 170–182.